Synergistic Effects of TeO₂-SeO₂ in Hydroxyapatite Coatings: A Dual Approach to Combat Inflammation and Infection

P. S. Shaji, S. Mathai*

PG and Research Department of Chemistry, Mar Ivanios College (Autonomous), Nalanchira, P.O, Thiruvananthapuram-695015, Kerala, India

Abstract

This paper introduced the temperature-controlled thermal decomposition method to provide unique nanostructured TeO₂-SeO₂-HAp coatings on Ti substrates. The mechanical and biological studies, including anti-bacterial and non-cytotoxic properties, are established under various simulated scenarios. In vitro, results indicated that the TeO₂-SeO₂-HAp coating has excellent adhesion strength and bioactivity. In addition, introducing nano TeO₂-SeO₂-HAp coatings inhibits the growth of gram-positive bacteria (*Staphylococcus aureus*) and gram-negative bacteria (*Escherichia coli*), without resorting to antibiotics. TeO₂-SeO₂ samples have only 75.99 % inflammation at 200 µg/mL and show excellent anti-inflammatory properties. The TeO₂-SeO₂-HAp coating reasonably showed good *in vitro* anti-bacterial as well as anti-inflammatory properties with no significant reduction in cell viability, i.e., at lower dosages of up to 83.09 g/mL. This shows a proof-of-concept for a TeO₂-SeO₂-HAp coating as a potential non-toxic anti-infective barrier for orthopedic implants with enhanced bio-mechano-functionalities.

Keywords: Sodium tellurite; Sodium selenite; Anti-inflammatory; Cytotoxicity; Porosity.

1. Introduction

The antibacterial properties of the orthopedic implants could be significantly improved by surface coating with metal nanoparticles (NPs) or nanopolymers [1]. The coating of endophyte surfaces with various biocompatible materials that possess anti-bacterial qualities has been studied. Strong broad-spectrum anti-bacterial and anti-inflammatory activities without compromising biocompatibility concerns have drawn a lot of attention to certain metal oxide-based compounds [2]. Due to its remarkable biocompatibility, tellurium dioxide (TeO₂), a solid oxide of tellurium, has a wide variety of uses in the biomedical field. TeO₂, a less toxic chalcogen, has anti-leishmaniasis, anti-inflammatory, anti-atherosclerotic, and immunomodulatory qualities [3,4]. TeO₂ is often 2- to 10-fold less dangerous in biological research because it is physiologically reactive and interacts with live tissues in a certain way [5-7]. In contrast, selenium dioxide (SeO₂) is a member of the

---

Corresponding author: sujamathaikunnath@gmail.com

same group and a micronutrient vital to human health. It belongs to the family of selenoproteins and is vital to the physiology of bones because it promotes the growth of osteoblasts and osteoclasts. [8]. Lack of it can slow down the production of new bones and result in bone issues, including osteoporosis and osteoarthritis. [9]. It is a preferred in vitro agent because of its reduced toxicity and superior anti-bacterial, anti-infective, and antioxidant qualities for mammalian cells. SeO$_2$ was created and tested for use in biomedical applications. Its anti-inflammatory and anti-infective qualities were verified by both in vitro and in vivo investigations [10,11].

In the bone tissue of all vertebrates, nanohydroxyapatite [Ca$_{10}$(PO$_4$)$_6$(OH)$_2$], a bioceramic, is found in considerable amounts [12]. It is very helpful in biological applications where bone augmentation is required. Because of the speedy bone regeneration it induces by the rapid resorption of live cells from the substance, nanohydroxyapatite (HAp) has a structure similar to that of bone minerals, but it is also more soluble and biologically bioactive [13]. These exceptional attributes promote enhanced osteoblast adhesion and long-term viability [14]. TeO$_2$ and SeO$_2$ can be combined with nanoHAp to encourage bone formation, function as anti-infective and anti-inflammatory therapeutic agents, or even as anticancer therapeutic agents [15,16]. Based on the aforementioned factors, the (TeO$_2$-SeO$_2$) mixed nanocomposite coating is employed to increase the bioactivity of nano HAP, a non-toxic binder [17,18].

The thermal decomposition process is used to create homogenous nanocomposite materials in order to make such composite coatings [19,20]. The main focus of the current investigation is the development of (TeO$_2$-SeO$_2$) in combination with nano HAp composite coating by a thermal decomposition procedure. The mechanical, biochemical, and biological qualities, including anti-bacterial and non-cytotoxic properties, are established via additional assessments under various simulated scenarios. This made it possible to forecast that the mixed composite covering and metal substrate would adhere strongly. This attempts to thoroughly understand the new approaches for using titanium substrates as bio-implants. This nanocomposite is anticipated to be produced at a very low temperature, using low-cost technology, a straightforward approach, and homogeneous and regulated coatings with microstructural homogeneity.

2. Material and Methods

2.1. *Materials*

Commercially available pure Ti specimens (Grade T3160) of area 2×1 cm^2 and 1 mm thickness were used as the coating substrate and purchased from Sigma Aldrich (Germany). They were mechanically polished using 36-grit SiC paper and rinsed with water, ethanol, and acetone for 15 min each. Tellurium (IV) chloride (TeCl$_4$, 99.9 %), Sigma Aldrich (Germany), Selenium (IV) chloride, SeCl$_4$, 99.9 %, Sigma Aldrich Germany, Germany), Isopropyl alcohol (IPA, 99.9 %, Sigma Aldrich, Germany) were used as the raw materials for the preparation of mixed oxide coatings. Calcium nitrate tetrahydrate, Ca(NO$_3$)$_2$·4H$_2$O (98 %, Spectrum, India), ammonium dihydrogen orthophosphate, NH$_4$H$_2$PO$_4$ (99 %,

Rankem, India), sodium hydrogen carbonate (purified), $NaHCO_3$ (99 %, Merk, India), dipotassium hydrogen orthophosphate, K_2HPO_4 (99.9 %, Fisher Scientific, Canada), magnesium chloride, $MgCl_2 \cdot 6H_2O$ (98 %, Nice, India), calcium chloride dehydrate, $CaCl_2 \cdot 2H_2O$ (97 %, Fisher Scientific, Canada), sodium sulfate anhydrous A.R., Na_2SO_4 (98 %, Merk, India), tris buffer AR, $(CH_2OH)_3CNH_2$ (99 %, Spectrum, India), sodium hydroxide pellets AR, (99 %, SRL, India) were used for the preparation of SBF in this study.

2.2. *Thermal decomposition method*

Tellurium(IV) chloride ($TeCl_4$) and selenium(IV) chloride ($SeCl_4$) were weighed accurately so that the total amount of the composite/cm^2 must be 10 mg. A slurry of 10 mL isopropanol solution was made to obtain the following composition: (a) 100 wt.% TeO_2, (b) 80 wt.% TeO_2 + 15 wt.% SeO_2 + 5 wt.% HAp and (c) 60 wt.% TeO_2 + 40 wt.% SeO_2 has been prepared to develop TeO_2, TeO_2- SeO_2- HAp, TeO_2- SeO_2 nanocomposite coatings having both adhesion strength and bioactivity. The mixed oxide solution was applied to the pretreated Ti substrates and was dried at 65 °C for 30 min. Finally, the coatings were sintered at 700 °C for half an hour and cooled [21]. The prepared mixed oxide coatings were chosen for alkaline treatment in 5 M NaOH at 60 °C for 24 h followed by biomimetic growth in Kukubo's 1.5 simulated body fluid (SBF) for 14 days at 36.5 °C.

2.3. *Porosity*

The porosity of TeO_2, TeO_2- SeO_2, TeO_2- SeO_2- HAp mixed oxide nanocomposite coating was determined using the equation:

$$Porosity = \frac{Wbj - Wb}{Wp} \times 100\%$$

where W_p = sample weight before coating, W_b = sample weight after coating, and W_{bj} = sample weight after immersion in SBF solution [22].

2.4. *Electrochemical evaluation*

Electrochemical impedance spectroscopy (EIS) and cyclic voltammetry (CV) in a 0.9 % NaCl solution were used to examine the electrochemical behavior of nanocomposite coatings that had been produced on Ti. Electrochemical investigations were carried out in a typical three-electrode cell. Ti served as the working electrode for all measurements, with the saturated calomel electrode (SCE) and the platinum (Pt) electrode serving as the reference and counter electrodes. Utilizing Metrohm Autolab PGSTAT204 equipment (India), all electrochemical experiments were carried out in an electrochemical workstation (EIS and CV). The potential range used for the EIS measurements was -1.0 V to 1.0 V. Each experiment was done three times to ensure repeatability before the data was collected using internal software (Autolab). The mixture was left undisturbed, and a CV was made.

2.5. *Evaluation of in vitro bioactivity*

In 1.5 Kukubo's simulated body fluid (SBF) over 14 days at 36.5 °C (pH: 7.4), the *in vitro* mineralization for bioactivity of the created coatings may be investigated. Following that, the specimens were immersed in 20 mL of an acellular simulated bodily fluid (1.5 SBF) with the following chemical components: Na^+: 213.0 K^+: 7.5 Mg^{2+}: 2.3 Ca^{2+}: 3.8 Cl^-: 221.7 HCO^{3-}: 221.7 HPO_4^-: 6.3 SO_4^{2-}: 0.8 mmol/L at 36.5 ºC and pH 7.4 [23,24]. The appropriate quantity of reagent-grade ingredients, including distilled water, 1.0 M HCl, $CaCl_2$, Na_2SO_4, $MgCl_2$, and $NaHCO_3$, were dissolved to form the SBF solution. Tris-hydroxymethyl aminomethane $((CH_2OH)_3CNH_2)$ was then used to buffer the pH. Microscopically and spectroscopically analyzed coating porosity, crystallinity, chemical composition, microstructural morphology, and surface roughness both before and after the mineralization investigation. The phase purity of the synthetic coating materials was evaluated using X-ray diffraction (XRD, Bruker D8 ADVANCE with DAVINCI design, India). Phase identification was completed by comparing the peak locations of the diffraction patterns with ICDD (JCPDS) standards. Fourier transform infrared spectroscopy (Thermoscientific Nicolet iS50, India) was used to identify the chemical functional groups. FTIR spectra between 400 and 4000 cm^{-1} were recorded. With the help of a scanning electron microscope (SEM, Carl Zeiss EVO 18 Research, India), surface morphological investigations were performed. The surface roughness morphology of the coatings was studied by employing the Nanosurf Flex-ANA instruments (India) for atomic force microscopy (AFM).

2.6. *In vitro anti-bacterial test*

The produced TeO₂-SeO₂ nanocomposite coatings were studied using the usual disc diffusion technique, which has been slightly modified and is reported in the European Pharmacopoeia [25]. Both Gram-positive (*Bacillus subtilis* MNN 2111 and *Staphylococcus aureus* MTCC 96) and Gram-negative (*Pseudomonas aeruginosa* ATCC 27853 and *Escherichia coli* MTCC 443) bacteria were used in the test, which was carried out using bacterial stock cultures from Biovent Innovations Pvt Ltd. To assess the sample's anti-bacterial activity, concentrations of 0.625, 1.25, 2.5, and 5 mg/mL were used. 0.05 % DMSO was employed as the adverse drug, while streptomycin 0.125 mg/mL was used as the reference drug (positive control). Mueller Hinton agar (MHA) sterile plates were used for the experiment. Freshly subcultured bacterial strains were suspended in 1 mL of nutrient solution and incubated for 2 h at 37 °C to produce log-phase cultures. The opacity of the cultures was assessed using 0.5 McFarland turbidity standards, which equates to 1 to 2 108 colony-forming units per milliliter. Using a sterile swab, 100 L of the pure cultures of the test strains were uniformly swabbed over the surface of the MHA plate to establish an equivalent inoculum. After allowing the plates to dry for five minutes, DMSO, standard drug-containing discs, and various sample concentrations were added to the MHA plates. Following a 24 h incubation period at 37 °C, the anti-bacterial activity was identified and the well's zone of inhibition was measured in millimeters [26].

2.7. *In vitro anti-inflammatory activity*

The reaction mixture (0.5 mL) consisted of 0.4 mL bovine serum albumin (1 % aqueous solution) and varying test sample concentrations. The samples were incubated at 37 ºC for 20 min, and 2.5 mL phosphate buffered saline (pH 6.3) was added to each tube and then heated at 57 ºC for 20 min [27,28]. The absorbance was measured using a spectrophotometer at 660 nm. The percentage inhibition of protein denaturation was calculated as follows:

Percentage of inhibition = [(Abs Control – Abs Sample) / Abs control)] ×100

2.8. *In vitro cytotoxicity test*

For MTT analysis, the normal fibroblastic cell line L929 (which has ISO certification) was chosen. The National Centre for Cell Culture (NCCS), located in Pune, India, was where the cell-lines were bought. The cell lines were kept alive in T-25 tissue culture flasks with an antibiotic solution comprising Penicillin (100 g/mL), Streptomycin (100 g/mL), and Amphotericin B (2.5 g/mL) and DMEM supplemented with 10 % FBS. Cell lines were cultured and stored at 37 °C in an incubator with 5 % CO_2 that was humidified (NBS Eppendorf, Germany). Confluent flasks were trypsinized using 500 L of 0.025% trypsin in PBS containing 0.5 mM EDTA solution and then centrifuged at 1500 rpm for five minutes at room temperature. After the supernatant was discarded, the pellet was resuspended in the necessary amount of DMEM for subculturing, freezing, or seeding on well plates for assay experiments. From a stock of 1 mg/mL DMSO (0.5 %), five distinct concentrations (6.25 g/mL, 12.5 g/mL, 25 g/mL, 50 g/mL, and 100 g/mL) were created. 1 mL of sterile PBS was used to dissolve 5 mg of MTT powder. 20 L of MTT and 80 L of DMEM were combined to make 100 L of 20 % MTT solution. The finished MTT was stored in darkness [29]. 5000 cells/well in 100 L of medium (DMEM) were put into each well of a 96-well ELISA plate. PBS buffer was placed in the 96-well ELISA plate's outermost wells to stop the material from evaporating. The plates were incubated for 24 h at 37 °C in a humidified 5 % CO_2 incubator. Plates were removed after incubation, and the used medium was thrown away. 100 L of the sample was introduced to the appropriate wells at various concentrations. 100 L of DMEM with 0.5% DMSO was added to the negative control wells, and 100 L of the standard medication doxorubicin was added to the positive control wells. Triple samples were analyzed. The medium was withdrawn after 24 h of incubation, and the wells were then cleaned with 100 L of PBS buffer. Immediately after the PBS was removed, 100 L of MTT dye was added. Incubation took place in the dark for two hours. The absorbance was measured at 570 nm using a microplate reader (Thermoscientific Multiskan Go version 1.00.40), and the percentage viability was calculated using a formula.

$$\% \text{ Viability} = \frac{\text{OD of the test}}{\text{OD of the control}} \times 100$$

The IC_{50} value is the half-maximal inhibitory concentration of the sample. The IC_{50} values were calculated using the equation for slope (y = mx + C) obtained by plotting the average absorbance of the different concentrations of the test sample (6.25-100 µg/mL), where OD is the optical density.

3. Results and Discussion

3.1. *Physico-chemical characterization*

3.1.1. *Porosity*

Table 1 displays the findings of the porosity of the TeO_2, TeO_2-SeO_2, TeO_2-SeO_2-HAp nanocomposites coatings. It is evident from the results of the porosity tests that TeO_2 induces a reduction in porosity. With the addition of SeO_2 and HAp content in the TeO_2-SeO_2-HAp nanocomposite coating, the porosity of the coatings increases. The TeO_2-SeO_2-HAp nanocomposite coating in this investigation had the maximum porosity. Porosity in nanocomposites may harm their mechanical performance, but since it greatly increases the materials' bioactivity, it might be crucial for biological applications. This improvement could be ascribed to the physiological fluids' capacity to pass through the holes in the nanocomposites, enabling the formation of a TeO_2-SeO_2-HAp-like layer of crystals on their surface and stronger bioactive activity. As a result, implants with large fissures and high porosity will speed up osseointegration and promote bone regeneration [30,31].

Table 1. Porosity of TeO_2, TeO_2-SeO_2, TeO_2-SeO_2-HAp nanocomposite coating.

SL. No.	Samples	Porosity%
1	TeO_2	1.72
2	TeO_2-SeO_2	3.17
3	TeO_2-SeO_2-HAp	4.60

3.1.2. *X-ray diffraction (XRD)*

Fig. 1 depicts the XRD patterns of the TeO_2, TeO_2-SeO_2, and TeO_2-SeO_2-HAp coatings after being exposed to SBF solution for 14 days at 36.5°C (pH: 7.4) and after being treated with NaOH on Ti substrate. Fig. 1a displays the primary peaks that resulted, which are typical tetragonal phase TeO_2 peaks at 2θ = 27.459º, 36.080º, and 41.249º. The production of Na_2O is what causes the peak at 54.337º. The outcome suggests that after being exposed to NaOH solutions, sodium metatellurite (Na_2TeO_3) crystallized on the surface of Ti metal. After being submerged in SBF for 14 days, the coating exhibits classic hydroxyapatite peak appearances at 28.104°, 31.679°, and 56.663°. The detected diffraction peaks match the data from the relevant standard literature (42-1365 in the PDF card) [32]. The orthorhombic phase of TeO_2 is represented by a small sharp peak at 2θ = 27.447º and a large peak at 2θ =38.348º in Fig. 1b. SeO_2, which was in good accord with the PDF card number 11-069331, is responsible for the wide peak at 2θ =40.139°. The production of Na_2O upon treatment

with NaOH is responsible for the prominent peaks at 52.955º and 54.313º. The coating displays distinctive peaks at 36.069º and 56.630º, indicating HAp is crystalline. The creation of a crystalline sodium tellurite-sodium selenite-HAp nanocomposite coating on the surface of the Ti metal following treatment with NaOH solutions is the cause of these observed distinctive peaks. The tetragonal phase (TeO_2) is shown by a sharp peak at 2θ = 27.360º and a wide peak at 35.991º in Fig. 1c. SeO_2 is responsible for the wide peak at 41.159º, while the distinctive peaks at 54.262º and 56.598º are caused by the production of Na_2O following treatment with NaOH. The coating displays distinctive peaks at 36.069°, 41.159°, and 56.630°, indicating that HAp is crystalline in nature. The creation of a crystalline sodium tellurite-sodium selenite-HAp nanocomposite coating on the surface of the Ti metal upon treatment with NaOH is the cause of these observed distinct peaks. Sufficiently negatively charged Te-OH and Se-OH groups may cover the surface of the alkaline-treated TeO_2, TeO_2-SeO_2, and TeO_2-SeO_2-HAp coated substrates when they are immersed in SBF solution. One way to explain the mechanism would be as follows: When SeO_2 is treated with alkali, it yields sodium selenite, but TeO_2 yields sodium tellurite. The equation is represented as:

$$TeO_2 + 2NaOH \rightarrow Na_2TeO_3 + H_2O$$
$$SeO_2 + 2NaOH \rightarrow Na_2SeO_3 + H_2O$$
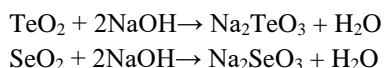
After alkaline treatment and immersion in SBF solution, Ca^{2+} and PO_4^{3-} ions frequently precipitate rapidly on the surfaces of nanocomposite samples. The negative charge on the surface of the nanocomposite is essential for the creation of bone-like apatite because it attracts the negative charge on the positive Ca^{2+} ions from the SBF solution. Conversely, PO_4^{3-} groups gravitate rapidly toward positively charged materials. Longer immersion times further result in the production of apatite nucleation sites when they are exposed to SBF [33]. The formation of a bone-like layer with high bioactivity, fair degradability, and moderate durability on the surfaces of coated samples was mostly influenced by their bioactive behavior after being treated with 5 M NaOH and immersed in SBF, as predicted [34,35].

During immersion in SBF, more calcium (Ca^{2+}) and phosphorus (PO_4^{3-}) ions are produced, indicating the formation of bone-like apatite. This result is in line with past investigations on the bioactivity of coatings based on HAp. Moreover, the peaks at (200) and (212) indicated crystalline simple tetragonal SeO_2, which was consistent with findings that had already been published [36,37]. The reflection from the (102) crystal plane, which results in a significant diffraction peak, indicates that TeO_2 has grown with a strong preferred orientation. When HAp groups, sodium tellurite, and sodium selenite are introduced, the ability of the nanocomposite specimens to adhere to bone is improved. It's also critical to remember that bioceramics need to be mineralized with apatite to maintain their bioactivity and promote integration with the host bone [38]. As a result, dental implants and artificial bones may be employed extensively.
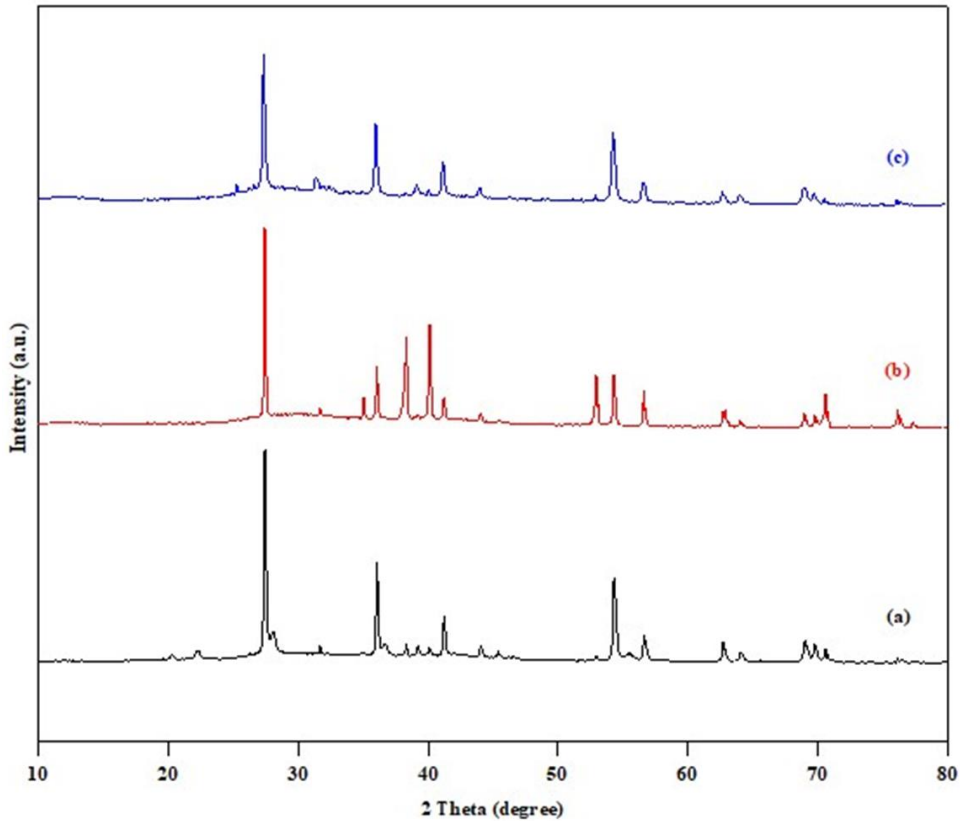
Fig. 1. XRD patterns of (a) TeO₂ coating, (b) TeO₂-SeO₂ nanocomposite coating, and (c) TeO₂-SeO₂-HAp nanocomposite coating on Ti substrate treated with NaOH and after immersion in SBF for 14 days at 36.5 °C.

3.1.3 *Fourier transform infrared (FTIR) spectroscopy*

Fig. 2 displays the FTIR spectra of the nanocomposite TeO_2, TeO_2-SeO_2, and TeO_2-SeO_2-HAp coating on Ti after treatment in 5 M NaOH. Fig. 2a illustrates the FTIR transmission bands associated with the hydroxyl-sodium (Na-OH) stretching vibration of the hydroxyl group and hydrogen bond [39,40], which occur about 2161.20, 1980.54, and 1685.30 cm⁻¹. Two absorption bands of Te-O-Te or O-Te-O linkages (-TeO_2) with Na-O are ascribed to the bands at the optically visible range of 846.05 cm⁻¹ and 514.25 cm⁻¹ [41]. These findings showed that the surface of the Ti metal strip crystallizes TeO_2 into sodium tellurite (Na_2TeO_3) through a reaction with NaOH. Fig. 2b represents the characteristic absorption bands in 3449.87 cm⁻¹ and 3052.82 cm⁻¹ is due to the O-H stretching and bending of the water molecules, respectively [42]. The sodium hydroxyl group's stretching vibration bonds are what cause the band at 1654.29 cm⁻¹. Te=O and Se=O (metal oxide) stretching absorption bands have been discovered in the 1377 - 468 cm⁻¹ range [43]. Because of the

stretching caused by Se=O, a strong and precise absorption band was discovered at 846.41 cm^{-1}. The bending vibration of Te-O bonding is the band at 496.56 cm^{-1}. The research showed that sodium tellurite-selenite (Na_2TeO_3-Na_2SeO_3) treated with 5 M NaOH formed with structural integrity. Fig. 2c represents the characteristic absorption bands in 3453.77 cm^{-1} and 3049.24 cm^{-1} due to the O-H stretching and bending of the water molecules, respectively. The sodium hydroxyl group's stretching vibration bonds are what cause the band at 1685.30 cm^{-1}. Se=O stretching absorption bands were discovered in the 1443.64 cm^{-1}. Se=O stretching was discovered to provide a strong absorption band at 846.94 cm^{-1}, while Te-O bond bending vibration was found to cause a band at 496.56 cm^{-1}.
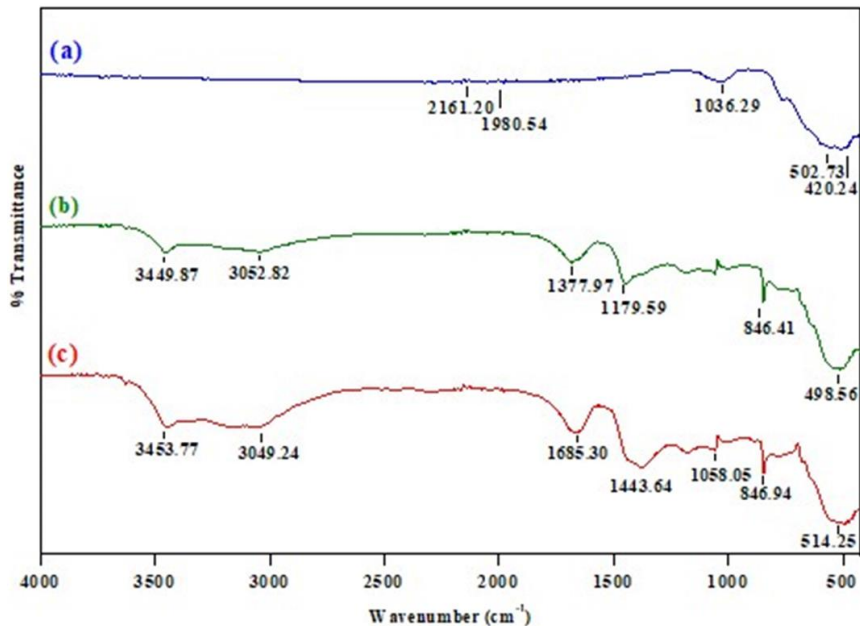
Fig. 2. FTIR image of (a) TeO_2 coating, (b) TeO_2-SeO_2 nanocomposite coating, and (c) TeO_2-SeO_2-HAp nanocomposite coating on Ti substrate treated with 5 M NaOH.

Figs. 3a-c shows the FTIR spectrum of the Ti samples of TeO_2, TeO_2-SeO_2 and TeO_2-SeO_2-HAp nanocomposite coating treated in 5 M NaOH and after immersion in SBF for 14 days at 36.5 °C (pH: 7.4). Fig. 3a represents the FTIR transmission bands occur around 2161.51 and 1657.07 cm^{-1} belong to the hydroxyl-sodium (Na-OH) stretching vibration of the hydroxyl group and hydrogen bond [44]. A broad peak is for HAp at 1046.30 cm^{-1}. The strong peaks at 487.29 cm^{-1} were similar to the absorption bands of α-TeO_2. Fig. 3b represents the characteristic absorption bands in 2182.97 cm^{-1} and 2046.83 cm^{-1} due to the O-H stretching and bending of the water molecules, respectively. The band at 1654.00 cm^{-1} is due to the stretching vibration bonds of the sodium hydroxyl group and Se=O stretching absorption bands [45]. A sharp band at 482.71 cm^{-1} is the bending vibration of Te-O bonds and may be due to the formation of a phosphate ion group in HAp. Fig. 3c shows the bands 3726.37 cm^{-1}, 2161.29 cm^{-1}, 2034.07 cm^{-1} and 2016.19 cm^{-1} corresponds to OH stretching

vibration. In concordance with the stretching vibration of Na-OH, the peaks at 1653.70 cm^{-1}. The phosphate ion group (PO$_4^{3-}$), whose absorption peak is at 1981.23 and 482.70 cm^{-1}, is what causes this absorption. The vibrations of TeO$_3$, TeO$_4$, and Te-O-Te or O-Te-O links with Na-O, respectively, are assigned to the bands at 459.85 cm^{-1} and 407.90 cm^{-1}.
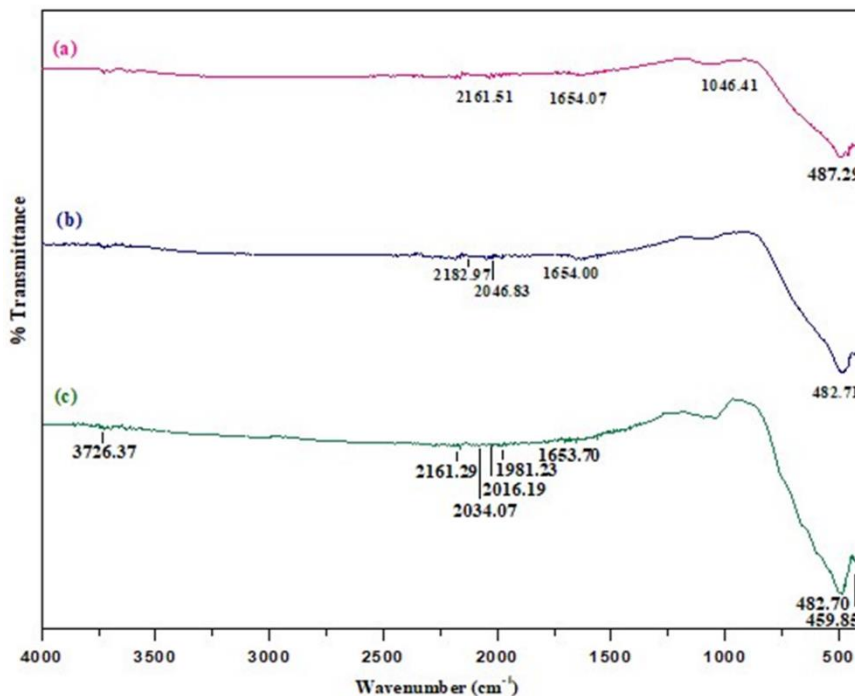

Fig. 3. FTIR image of (a) TeO$_2$ coating, (b) TeO$_2$-SeO$_2$ nanocomposite coating, and (c) TeO$_2$-SeO$_2$-HAp nanocomposite coating on Ti substrate treated with NaOH and after immersion in SBF for 14 days at 36.5 °C.

3.2. *Electrochemical investigation*

3.2.1. *Cyclic voltammetry (CV)*

Fig. 4 represents a cyclic voltammogram of TeO$_2$-SeO$_2$-HAp nanocomposite coating on Ti substrate that was performed in a typical three-electrode electrochemical cell over a range of -1.0 to 1.0 V in a solution of 0.9 % NaCl solution. Fig. 4a shows the cyclic voltammograms of TeO$_2$-SeO$_2$-HAp nanocomposite coating treated with 5 M NaOH on a Ti substrate. It was observed that the electrochemical reaction of electroactive species in the electrolytic solution started to occur at about -0.1 V. From -1.0 V to -0.25 V, a plateau in current density was seen that was consistent with the mass transport-controlled mechanism. On a Ti substrate, a TeO$_2$-SeO$_2$-HAp nanocomposite coating was exposed to SBF for 14 days at 36.5 °C after being treated with 5 M NaOH, as shown in Fig. 4b. Between -1.0 V and 1.0 V, a sharp rise in current density was noticed. This correlates to Ca^{2+} and

PO_4^{3-} deposition in the coating system during biomimetic growth. At a potential > 0.5 V, the evolution of hydrogen was the predominant reaction, and scanning revealed many bubbles at the Ti surface. From these findings, it can be concluded that the desirable potential range for good nanocomposite coatings on Ti substrate without the interference of hydrogen evolution is between -0.9 V and 0.5 V. In vitro, electrochemical testing was used to further investigate the bioactive behavior of the nanocomposite coatings. To illustrate the significance of Ti metal having a bioactive layer in biomedical applications, the experiments were conducted on a Ti substrate. In this case, cyclic voltammetry (CV) was utilized to identify the reduction peaks that were present in the nanocomposite coating on the Ti substrate. Neither before nor after polarization was the decohesion of the coatings seen. This illustrates how well the coating adheres to the body and resists corrosion in the physiological milieu following implantation. TeO_2 and SeO_2 nanoparticles at the coating interface are strongly held together by the nanometer-thick native oxide layer already on the Ti substrate.
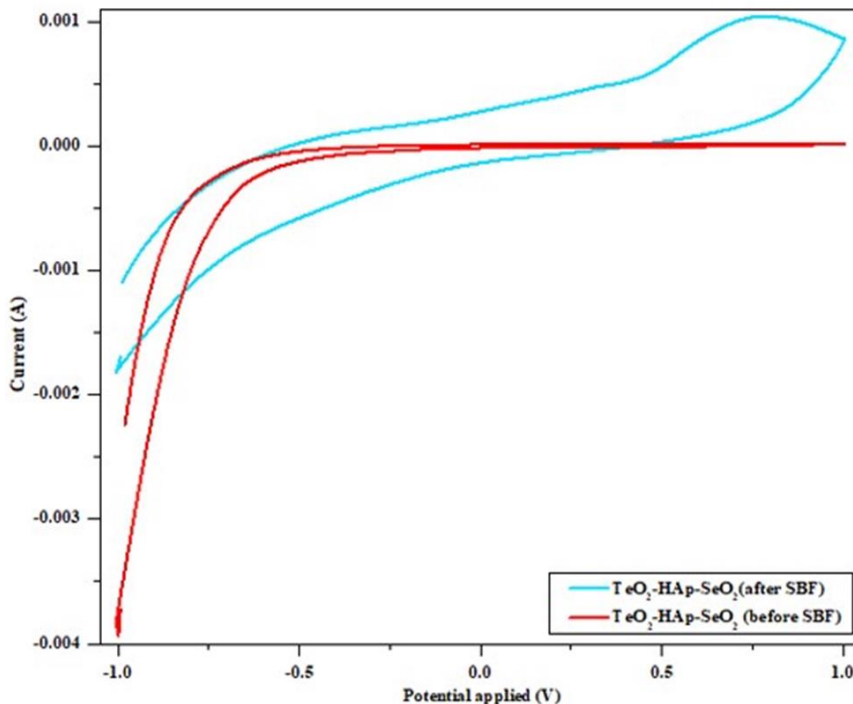

Fig. 4. Cyclic voltammograms of (a) TeO_2-SeO_2-HAp nanocomposite coating treated with 5 M NaOH and (b) TeO_2-SeO_2-HAp nanocomposite coating after alkaline treatment and immersion in SBF for 14 days at 36.7 °C.

3.2.2. *Electrochemical impedance spectroscopy (EIS)*

Fig. 5 displays the bode plot of the TeO_2-SeO_2-HAp nanocomposite coatings on Ti in 0.9% NaCl. EIS spectra of the nanocomposite coated Ti strips in SBF were analyzed, and the

resultant data was fitted Randle's equivalent circuit model $[R_s(R_1(C_2(R_2C_2)]$, where R_s, R_1, R_2 are the solution resistance, polarization resistance in the high-frequency domain (HF) and polarization resistance (R_p) in the low-frequency domain (LF) respectively. Similarly, C_1 and C_2 are the constant phase elements (CPEs) in the HF domain and LF domain, respectively. The R_1, C_1 for TeO₂-SeO₂-HAp (before immersion in SBF) showed 77.234 Ωcm^2 and 6.58×10^{-8} F and that TeO₂-SeO₂-HAp (after immersion in SBF) coated panel were 5081.8 Ωcm^2 and 3.17 Ωcm^2 respectively. Similarly, R_2 and C_2 for TeO₂-SeO₂-HAp (before immersion in SBF) was 7569.5 Ωcm^2 and 5.77×10^{-5} F, that of TeO₂-SeO₂-HAp (after immersion in SBF) were 9356.1 Ωcm^2 and 1.90×10^{-5} F respectively. Ti rust resistance is enhanced by the HAp coating over TeO₂-SeO₂, as seen by the lower CPE and greater R_P. The HF and LF results clearly demonstrated that the HAp treatment improves the polarization resistance of the coatings' internal and surface layers. When the Ti surface comes into contact with the SBF, the samples' high impedance values show that its passive oxide film protective function increases [46]. This may explain why the higher the R_p value, the lower the corrosion rate and the lower the ion release, resulting in higher corrosion resistance in TeO₂-SeO₂-HAp due to the deposition of Ca^{2+} and PO_4^{3-} ions after immersion in SBF. Bode plots of EIS of the nanocomposite coatings can be inferred, and more apatite could be induced on the surface due to long-term immersion in SBF solution. The nanocomposite coating could be charged negatively in a solution with a physiological pH of 7.4, attracting the positively charged Ca^{2+} ions, and then PO_4^{3-} groups in the SBF favoring apatite growth results in higher adhesion strength. The porous nature of the coating surface could favor osseointegration in the body environment.
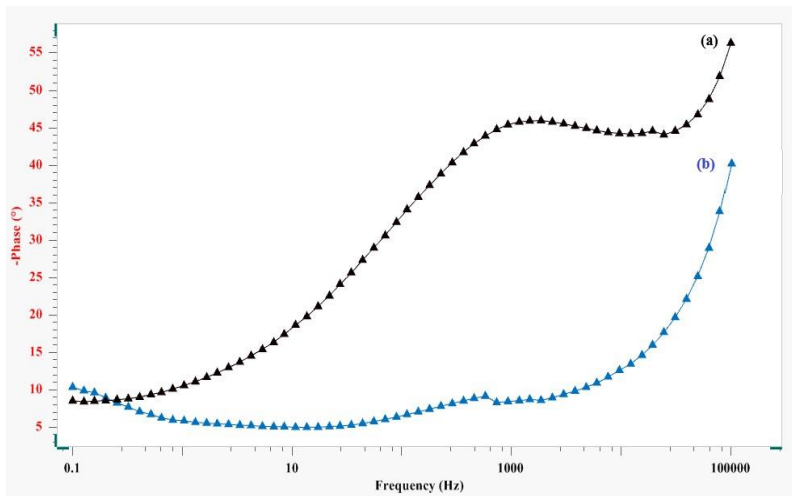

Fig. 5. Bode plot of (a) TeO₂-SeO₂-HAp nanocomposite coating treated with 5 M NaOH and (b) TeO₂-SeO₂-HAp nanocomposite coating treated with 5 M NaOH and after immersion in SBF for 14 days at 36.7 °C [pH: 7.4].

Table 2. The electrochemical impedance parameters of TeO_2-SeO_2-HAp nanocomposite coatings.

SL No.	Material	CPE_1 (F)	R_{P1} (Ω.cm^2)	Rs (Ω)	N	CPE_2 (F)	R_{P2} (Ω.cm^2)
1	TeO_2-SeO_2-HAp (before SBF)	6.58×10^{-8}	77.234	-20843	0.99175	5.77×10^{-7}	7569.5
2	TeO_2-SeO_2-HAp (after SBF	3.17×10^{-10}	5081.8	-25450	0.99324	1.90×10^{-7}	9356.1

3.3. *Evaluation of in vitro test for bioactivity*

3.3.1. *Scanning electron microscopy (SEM)*

The SEM micrograph of TeO_2, TeO_2-SeO_2, and TeO_2-SeO_2-HAp nanocomposite coating on Ti formed by thermal decomposition treated in 5 M NaOH and immersed in SBF solution for 14 days at 36.5 ºC is illustrated in Figs. 6-8. The SEM images shown in Fig. 6(a) show the surface morphology of TeO_2 treated with 5M NaOH coated on a Ti strip. It can be observed that the sodium tellurite layer is formed on the surface, which exhibits a typical expanded, frost pillar-like morphology. Fig. 6b shows the SEM image of the morphology of TeO_2 treated with 5 M NaOH and after immersion in SBF at 36.5 ºC (pH: 7.4) for 14 days. Due to the apatite layer that may be present on their surface, it seemed overcast and storm-like. Fig. 7a shows an SEM picture of a TeO_2-SeO_2 nanocomposite coating that has been treated with 5 M NaOH. The surface is packed with tiny pellet-like morphologies. In Fig. 7b is the TeO_2 -SeO_2 nanocomposite coating treated with 5 M NaOH, and after immersion in SBF for 14n days, the apatite is grown denser, which accelerates the nucleation and growth of Ca^{2+} and PO_4^{3-} ions. Fig. 8a is the TeO_2 -SeO_2-HAp nanocomposite coating on Ti treated with 5 M NaOH, which has a uniform with no major cracks and few pores identified, resulting in osseointegration in the body environment. Fig. 8b depicts an evenly aggregated layer on the surface with white precipitates on a TeO_2-SeO_2-HAp nanocomposite coating on Ti after it has been exposed to 5 M NaOH and SBF. This is caused by the high concentration of Ca^{2+} and PO_4^{3-} ions. This encourages continued cell growth and assures adherence, demonstrating great biocompatibility.

As apatite layers are formed by ion exchange in the SBF, the TeO_2-SeO_2-HAp nanocomposite coating on the Ti substrate exhibits various morphological changes on the surface. The ability of nanocomposite samples to form an apatite coating on their surfaces following immersion in SBF solution can be interpreted as evidence of their bioactivity. The results show that the whole surface of the nanocomposites was developed with an apatite, which is strong evidence that the composite was bioactive. This implies that a nanostructured surface composed of several small particles is necessary for the apatite crystallization process.
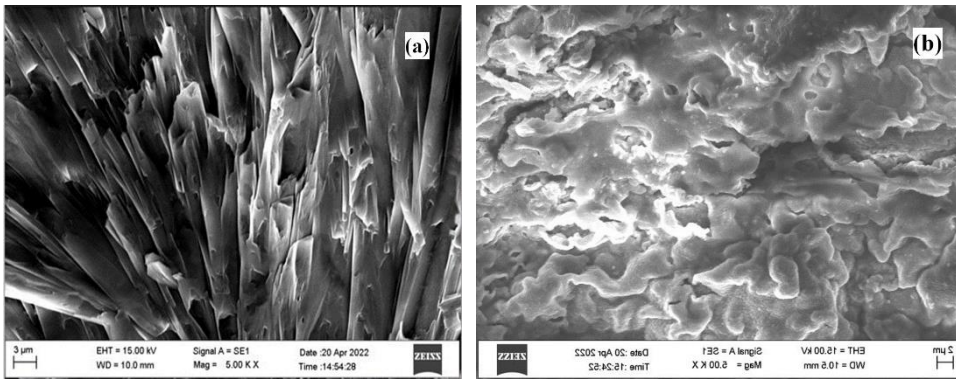
Fig. 6. SEM image of (a) TeO$_2$ coating treated with 5 M NaOH and (b) TeO$_2$ coating treated with 5 M NaOH and after immersion in SBF for 14 days at 36.5 °C [pH: 7.4].
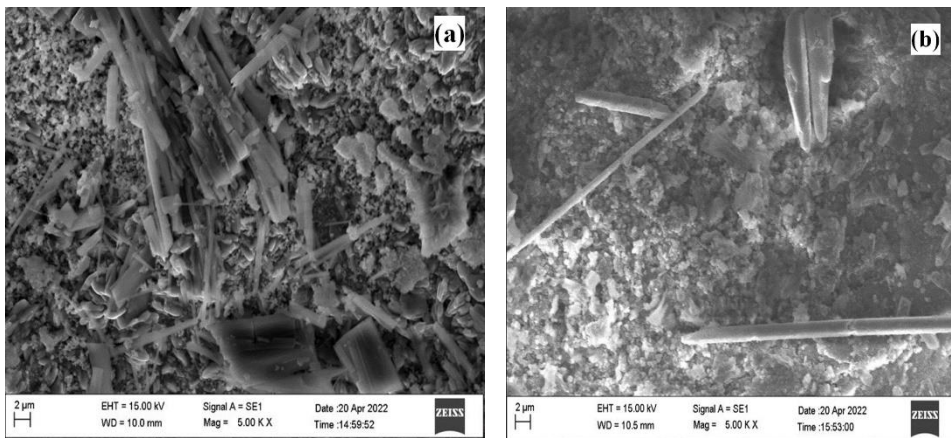

Fig. 7. SEM image of (a) TeO$_2$ -SeO$_2$ nanocomposite coating treated with 5 M NaOH, and (b) TeO$_2$ -SeO$_2$ nanocomposite coating treated with 5 M NaOH and after immersion in SBF for 14 days at 36.7 °C.
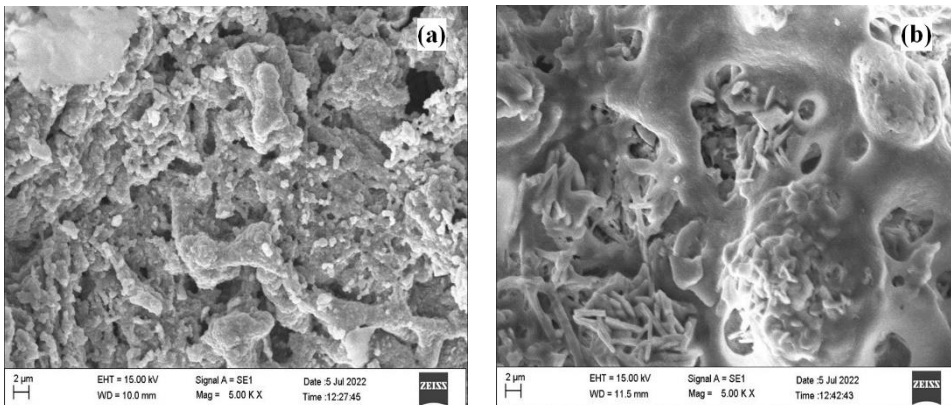

Fig. 8. SEM image of (a) TeO$_2$ -SeO$_2$-HAp nanocomposite coating treated with 5 M NaOH, and (b) TeO$_2$ -SeO$_2$-HAp nanocomposite coating treated with 5 M NaOH and after immersion in SBF for 14 days at 36.7 °C

3.3.2. Atomic force microscopy (AFM)

The AFM with three-dimensional images of TeO_2-SeO_2-HAp nanocomposite coatings is presented in Fig. 9. The image makes it evident that a thin covering of TeO_2, SeO_2, and HAp nanoparticles, with an average diameter of 47.21 nm, is present on the whole surface. The root-mean-square (RMS) roughness of the three-dimensional (3D) AFM picture in Fig. 9(a) of the TeO_2-SeO_2-HAp nanocomposite coating (before immersed in SBF) is 1.82 nm. The surface topography is depicted in Fig. 9 by the AFM picture of the coating taken prior to immersion in the SBF solution. Smaller and thinner coatings are discovered, with significantly smoother surface structures. Fig. 9b shows the AFM image of the coatings after biomimetic growth in SBF at pH 7.4 and 36.5 °C for 14 days. Rmax value decreased due to the formation of more HAp crystals on their surface. Fig. 10 shows the AFM image of the TeO_2-SeO_2-HAp nanocomposite coating treated with 5 M NaOH before and after immersion in SBF solution at pH:7.4 and 36.5 °C for 14 days describes that thin film with Rmax value 2.19 nm over the entire surface. Rmax values increased immersion due to the formation of more crystals of HAp, i.e., Ca^{2+} and PO_4^{3-} ions, on their surface.
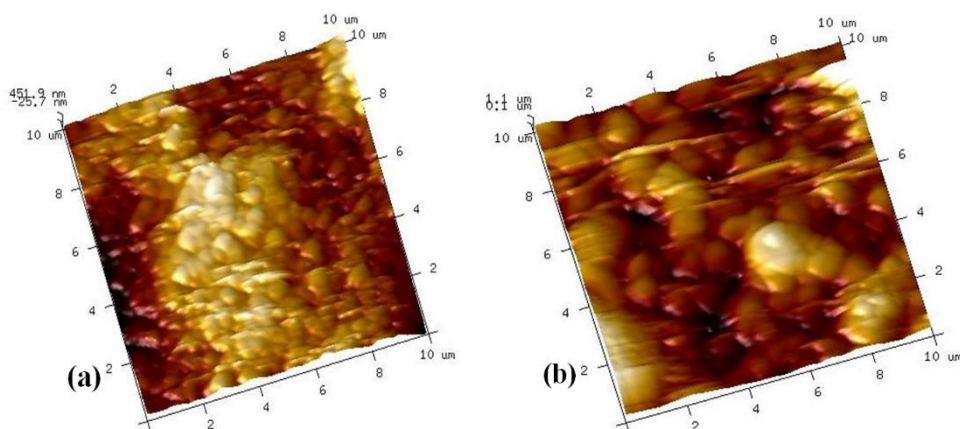

Fig. 9. AFM image of (a) TeO_2 -SeO_2-HAp nanocomposite coating treated with 5 M NaOH, and (b) TeO_2 -SeO_2-HAp nanocomposite coating treated with 5 M NaOH and after immersion in SBF for 14 days at 36.7 °C.

3.4. *In vitro anti-bacterial activity*

TeO_2-SeO_2 nanocomposites demonstrate significant anti-bacterial activity against *Bacillus subtilis, Staphylococcus aureus, Pseudomonas aeruginosa,* and *Escherichia coli*. Fig. 10 represents the anti-bacterial activities of different concentrations (0.62, 1.25, 2.5, and 5 mg/mL) of TeO_2-SeO_2 nanocomposite coating against four bacterial strains, where the zone of incubation takes place. The anti-bacterial activity with the highest inhibitory action of TeO_2-SeO_2 nanocomposite coating was against *Staphylococcus aureus* (Gram-positive) and *Escherichia coli* (Gram-negative), respectively, which is illustrated in Fig. 11. The clear area around the sample plates demonstrates the activity of the sample and the suppression

of the bacterial culture, which provides the effectiveness of the acquired samples anti-bacterial property. We may infer that the produced TeO$_2$-SeO$_2$ nanocomposite coating is a powerful anti-bacterial agent since the zone of inhibition is high higher concentrations of TeO$_2$-SeO$_2$ nanocomposite coating generated a longer lag phase in bacterial development, according to the anti-bacterial activity data. This was seen especially in *Staphylococcus aureus* and *Escherichia coli*. This implies that TeO$_2$ and SeO$_2$ nanocomposite coating on Ti substrates inhibits bacterial growth by delaying bacterial development. The results show that TeO$_2$-SeO$_2$ nanocomposite coatings have strong anti-bacterial qualities with negligible to no negative effects on normal human cells. The combined presence of TeO$_2$ and SeO$_2$ prevents the bacterium from growing. When it comes to treating infections in bone implants caused by *Staphylococcus aureus* and *Escherichia coli*, a coating with increased anti-bacterial activity combined with biocompatibility is a superior option [47].
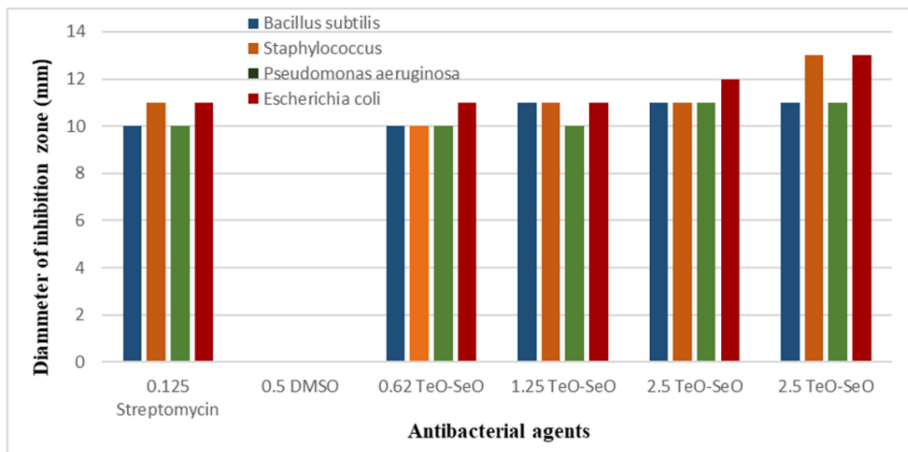

Fig. 10. Anti-bacterial activity of different concentrations of TeO$_2$-SeO$_2$ nanocomposite coating on Ti substrate with zone of inhibition against *Bacillus subtilis, Staphylococcus aureus, Pseudomonas aeruginosa, Escherichia coli.*

Fig. 11. Anti-bacterial activity of TeO$_2$-SeO$_2$ nanocomposite coating on Ti substrate with highest inhibitory action against *Staphylococcus aureus* and *Escherichia coli,* respectively.

3.5. *In vitro anti-inflammatory activity*

The anti-inflammatory activity of TeO_2-SeO_2 coating is shown in Fig. 12. For the TeO_2-SeO_2 sample, the concentration taken is 10-250 µg/mL TeO_2-SeO_2, i.e., the concentration at which 50 % inhibition is brought about (IC_{50} value) is 72.77 µg/mL. TeO_2-SeO_2 samples have 75.99 % inflammation at 200 µg/mL. From the results, the TeO_2-SeO_2 sample has the ability to destroy type III hypersensitivity class antigens, which cause inflammation. It proves that the TeO_2-SeO_2 sample has anti-denaturation ability. They are highly resistant to nonspecific protein and biomolecule deposition, or "biological fouling," as well as leukocyte adherence to the surfaces of biological materials as a result of their anti-inflammatory TeO_2-SeO_2 coating [48,49]. This thin-layer coating offers an increasingly important method of lowering the initial inflammatory response. This shows that the TeO_2 and SeO_2 nanocomposite coating on Ti substrates inhibits bacterial maturation, which stops bacterial growth and eliminates irritation.
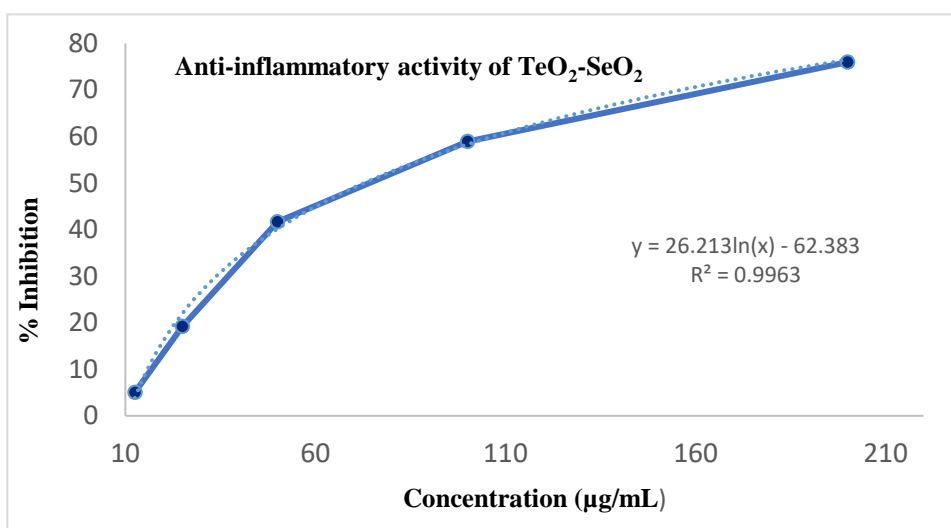

Fig. 12. Anti-inflammatory activity of TeO_2-SeO_2 coating.

3.6. *In Vitro cytotoxicity test*

In this study, the in vitro cytotoxicity of TeO_2-SeO_2 nanocomposite coating with normal fibroblast cells was evaluated by MTT assay using different concentrations. After in vitro cytotoxicity tests, from Fig. 13, it was found that fibroblast cells had grown over the surface of the TeO_2-SeO_2 nanocomposite coating on Ti. When the cells were incubated with test substances for 24 + 1 h, the fibroblast maintained its spindle forms and did not rupture. Different doses of the material (6.25-100 g/mL) were supplied to the cells, and a dose-dependent decrease in cell viability was seen. According to this MTT test study on the L929 cell line, fibroblast cells treated with TeO_2-SeO_2 nanocomposite coating on Ti substrate at concentrations of 6.25 to 50 g/mL did not experience any discernible toxicity (Fig. 13). The

IC$_{50}$ value was obtained as 83.09 µg/mL of the sample (Fig. 14). From Figs. 14 and 15, this *in vitro* investigation showed that the produced TeO$_2$-SeO$_2$-HAp nanocomposite coating is compatible with typical human fibroblast cells at lower dosages, i.e., up to 83.09 g/mL, and demonstrates modest cytotoxicity at higher levels (above 83.09 g/mL). Regular fibroblasts were used in in vitro cytotoxicity experiments to test the cytotoxicity of TeO$_2$-SeO$_2$ nanocomposite coatings on mammalian cells. MTT test results for nanoparticle doses between 6.25 and 83.09 g/mL showed no detectable cytotoxicity.
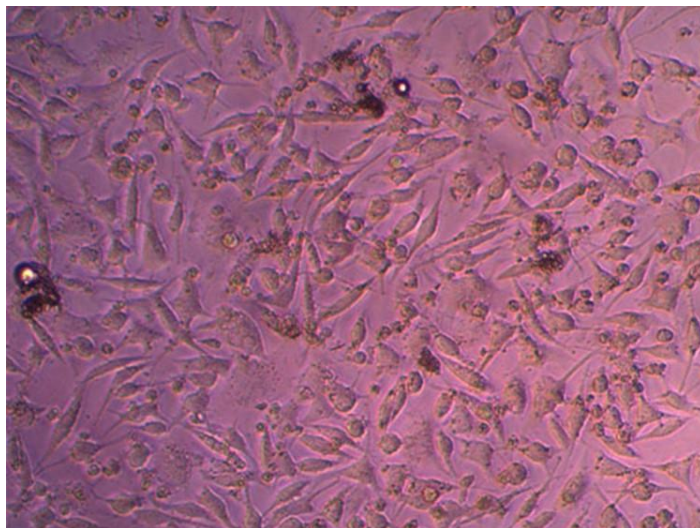

Fig. 13. Cytotoxicity activity in L929 of TeO$_2$-SeO$_2$ nanocomposite coating on Ti substrate.
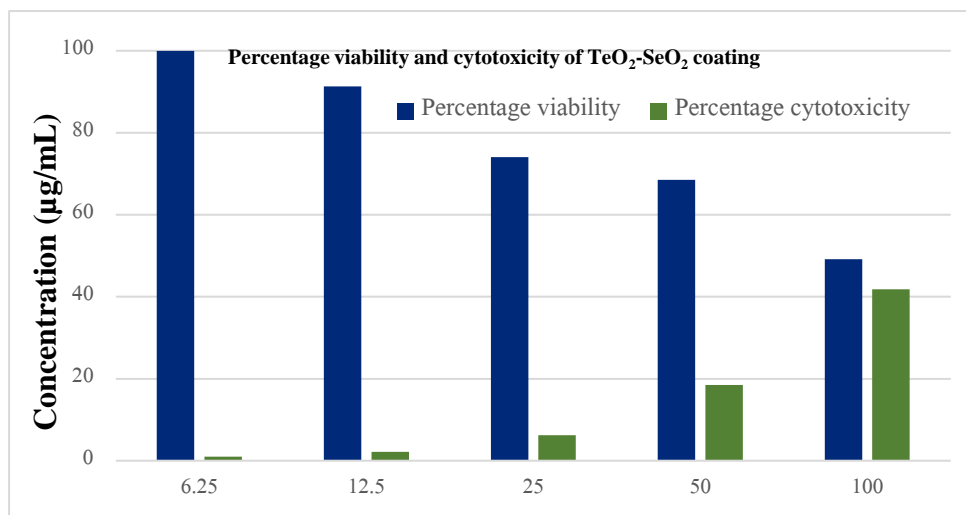

Fig. 14. Percentage of viability and MTT assay for varying concentrations of the test sample on L929 cell line TeO$_2$-SeO$_2$ nanocomposite coating on Ti.
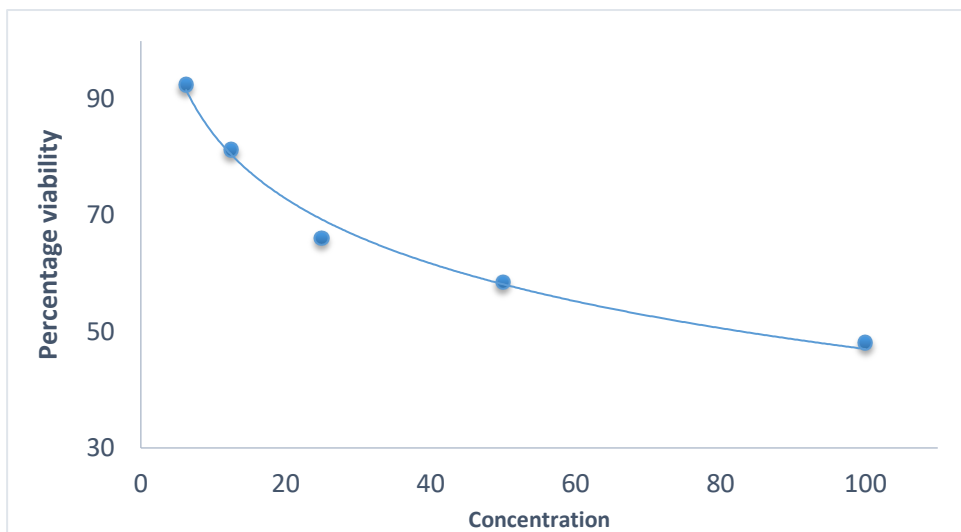
Fig. 15. Determination of cytotoxic activity of TeO_2-SeO_2 nanocomposite coating on Ti substrate.

4. Conclusion

The thermal decomposition approach may be used to create high-purity TeO_2-SeO_2-HAp nanocomposite coatings. The XRD, FTIR, SEM, and AFM analyses after SBF treatment supported the improved apatite forming capacity of the nanocomposite-covered Ti substrate. TeO_2-SeO_2-HAp coated Ti substrate revealed a noticeable biomimetic growth characteristic compared to TeO_2 and TeO_2-SeO_2 coated Ti substrate. The formation of new apatite crystals in SBF demonstrates that the tellurium dioxide and selenium oxide in the coating can increase the biological features of the coating, along with hydroxyapatite. The coating's excellent adhesiveness and ability to shield the Ti substrate from corrosion are indicated by the fact that there was neither detachment nor decohesion of the coating during surface potential change. With the development of TeO_2-SeO_2-HAp nanocomposite coating via the thermal decomposition method, a novel coating with multifunctional- anti-bacterial, and anti-inflammatory properties while having no harmful effects on normal human cells has been synthesized.

References

1. J. Sui, Y. Hou, M. Chen, Z. Zheng, X. Meng et al., Coatings **14**, ID 254 (2024). https://doi.org/10.3390/coatings14030254
2. H. Y. Ahmadabadi, K. Yu, and J. N. Kizhakkedathu, Colloidal. Surf. B. Biointerface **193**, ID 111116 (2020). https://doi.org/10.1016/j.colsurfb.2020.111116
3. H. Wang, L. Chai, Z. Xei, and H. Zhang, Chem. Res. Univ. **36**, 1 (2020). https://doi.org/10.1007/s40242-020-0193-0
4. B. Sredni, Semin. Cancer. Biol. **22**, 60 (2011). http://doi.org/10.1016/j.semcancer.2011.12.003
5. L. O. R. Cunha, I. E. Gouvea, and L. Juliano, An. Acad. Bras. Cienc. **81**, 15 (2009). http://doi.org/10.1590/s0001-37652009000300006

6. P. Tavakoli, F. Ghaffarifar, H. Telavari, A. KarimiPourSaryazdi, M. S. Dayer et al., Acta Parasitol. **67**, 143 (2022). https://doi.org/10.1007/s11686-021-00445-w
7. M. Doering, B. Diesel, M. C. Gruhlke, U. M. Viswanathan, D. Máníková et al., Tetrahedron **68**, 10577 (2012). https://doi.org/10.1016/j.tet.2012.09.021
8. H. Kim, K. Lee, J. M. Kim, M. Y. Kim, J-R Kim et al., Nat. Commun. **12**, 2258 (2021). http://doi.org/10.1038/s41467-021-22565-7
9. K. Hiraoka, S. Komiya, T. Hamada, M. Zenmyo, and A. Inoue, J. Orthop. Res. **19**, 809 (2001). https://doi.org/10.1016/S0736-0266(00)00079-6
10. H. Forootanfar, Adeli-sardou, M. Nikkhoo, M. Mehrabani et al., J. Trace. Elem. Med. Biol. **28**, 75 (2014). https://doi.org/10.1016/j.jtemb.2013.07.005
11. T. Adimulam, T. Arumugam, A. Foolchand, T. Ghazi, and A. A. Chuturgoon, Int. J. Mol. Sci. **22**, ID 12952 (2021). https://doi.org/10.3390/ijms222312952
12. N. Eliaz and N. Metoki, Materials **10**, 334 (2017). http://doi.org/10.3390/ma10040334
13. E. Fiume, G. Magnaterra, A. Rahdar, E. Verné, and F. Baino, Ceramics **4**, 542 (2021). https://doi.org/10.3390/ceramics4040039
14. N. Tran and T. J. Webster, Acta. Biomater. **7**, 1298 (2011). http://doi.org/10.1016/j.actbio.2010.10.004
15. C. L. Zhong, B. Y. Qin, X. Y. Xie, and Y. Bai, J. Nano. Res. **25**, 8 (2013). https://doi.org/10.4028/www.scientific.net/JNanoR.25.8
16. R. Karan, P. Manna, P. K. Maiti, and K. Das, J. Aust. Ceram. Soc. **56**, 1135 (2020). https://doi.org/10.1007/s41779-020-00459-z
17. S. Mondal, T. P. Nguyen, V. H. Pham, and G. Hoang, Ceram. Int. **46**, 3443 (2020). https://doi.org/10.1016/j.ceramint.2019.10.057
18. M. Prakasam, J. Locs, K. Salma-Ancane, D. Loca, A. Largeteau, and L. Berzina-Cimdina, J. Funct. Biomater. **6**, 1099 (2015). https://doi.org/10.3390/jfb6041099
19. W. Pang, X. Fan, K. Wang, Y. Chao, H. Xu et al., Nanomaterials **10**, 1039 (2020). https://doi.org/10.3390/nano10061039
20. X. Fu, Y. Zhu, J. Li, L. Jiang, X. Zhao, and X. Fan, Nanomaterials (Basel) **11**, 2374 (2021). https://doi.org/10.3390/nano11092374
21. T. Hesabizadeh, E. Hicks, D. M. Cruz, S. E. Bourdo, F. Watanabe et al., ACS. Omega **7**, 23685 (2022). https://doi.org/10.1021/acsomega.2c02316
22. Hartatiek, N. K. Fahmi, A. A. D. Putra, Y. Nasikhudin, J. Utomo et al., AIP Conf. Proc. **2234**, 040012 (2020). https://doi.org/10.1063/5.0008765
23. T. Kukobo and S. Yamaguchi, J. Biomed. Mater. Res. A **107** (2019). https://doi.org/10.1002/jbm.a.36620
24. Y. J. Wang, J. D. Chen, K. Wei, S. H. Zhang, and X. D. Wang, Mater. Lett. **60**, 3227 (2006). https://doi.org/10.1016/j.matlet.2006.02.077
25. Z. Bal, T. Kaito, F. Korkusuz, and H. Yoshikawa, Emerg. Mater. **3**, 521 (2020). https://doi.org/10.1007/s42247-019-00063-3
26. V. Thankamani, J. James, T. V. Arunkumar, and L. M. S. Dev, Int. J. Pharm. Res. Dev. **3**, 172 (2011).
27. H. Rahman, M. C. Eswaraiah, and A. M. Dutta, American-Eurasian J. Agric. amp; Environ. Sci. **15**, 115 (2015). http://doi.org/10.5829/idosi.aejaes.2015.115.121
28. S. Sakat, A. R. Juvekar, and M. N. Gambhire. Int. J. Pharma. Pharmacol. Sci. **2**, 146 (2010). http://doi.org/10.1055/s-0029-1234983
29. Y. Mizushima and M. Kobayashi, J. Pharma. Pharmacol. **20**, 169 (1968). https://doi.org/10.1111/j.2042-7158.1968.tb09718.x
30. Encinas-Romero, J. Peralta-Haley, J. J. Valenzuela-Garcia, and F. F. Castillon-Barrza, J. Biomater. Nano Biotech. **4**, 327 (2013). https://doi.org/10.4236/jbnb.2013.44041
31. C. Wu, W. Fan, Y. Zhuo, Y. Luo, M. Gelinsky et al., J. Mater. Chem. **22**, 12288 (2012). https://doi.org/10.1039/c2jm30566f
32. T. Mosmann, J. Immunol. Methods **65**, 55 (1983). http://doi.org/10.1016/0022-1759(83)90303-4

33. A. Fattah-alhosseini, S. S. Taheri, B. Z. Heydari, and P. S. Mohamadian, Int. J. Electrochem. **2011**, 9 (2011). https://doi.org/10.4061/2011/152143
34. S. Ni, J. Chang, and L. Chuo, J. Biomed. Mater. Res. A **196**, 205 (2005).
35. R. A. Youness, M. A. Taha, H. Elhaes, and M. Ibrahim, Mater. Chem. Phys. **190**, 209 (2017). https://doi.org/10.1016/j.matchemphys.2017.01.004
36. S. Xu, K. Lin, Z. Wang, J. Chang, L. Wang et al., Biomaterials **29**, 2588 (2008). https://doi.org/10.1016/j.biomaterials.2008.03.013
37. W. Xue, X. Liu, X. Zheng, and C. Ding, Biomaterials **26**, 3455 (2005). https://doi.org/10.1016/j.biomaterials.2004.09.027
38. L. L. Hench, Biomaterials **19**, 1417 (1998). https://doi.org/10.1016/S0142-9612(98)00133-1
39. U. Novak and J. Grdadolnik Spectrochim. Acta. A: Mol. Biomol. Spect. **253**, ID 119551 (2021). https://doi.org/10.1016/j.saa.2021.119551
40. Y. Gao, H. Lei, X. Yin, Y. Zhang, Z. Huang et al., ACS. Omega **8**, 7102 (2023). https://doi.org/10.1021/acsomega.2c08057
41. Pandarinath, G. Upender, K. N. Rao, and D. S. Babu, J. Non-Crystal. Solids **433**, 60 (2016). https://doi.org/10.1016/j.jnoncrysol.2015.11.028
42. F. Dai, Q. Zhuang, Ge Huang, H. Deng, X. Zhang, J. Coates et al., ACS. Omega **8**, 17064, (2023). https://doi.org/10.1021/acsomega.3c01336
43. J. C. Sabadel, P. Armand, D. Cachau-Herreillat, P. Baldedck, O. Doclot et al., J. Solid. State Chem. **132,** 411 (1997). https://doi.org/10.1006/jssc.1997.7499
44. M. Morssli, G. Cassanas, L. Bardet, B. Pauvert, and A. Terol, Spectrochim. Acta A: Mol. Spect. **47**, 529 (1991). https://doi.org/10.1016/0584-8539(91)80069-U
45. F. Tabatabaeian, E. Karimi, and M. Hashemi, Frontier. Chem. **10**, ID 904973 (2022). https://doi.org/10.3389/fchem.2022.904973
46. P. Bocchetta, L. -Y. Chen, J. D. C. Tardelli, A. C. dos Reis, F. Almeraya-Calderon, and P. Leo, Coatings **11**, 487 (2021). https://doi.org/10.3390/coatings11050487
47. J. Fernandes, T. Vaz, S. M. Gurav, and T. S. Anvekar, J. Sci. Res. **13**, 1043 (2021). https://doi.org/10.3329/jsr.v13i3.53740
48. H. Ghomi, M. H. Fathi, and H. Edris, Mater. Res. Bull. **47**, 3523 (2012). https://doi.org/10.1016/j.materresbull.2012.06.066
49. F. L. Yan, Z. R. Zhong, Y. Wang, Y. Feng, and C. H. Li, J. Nanobiotechnol. **18**, 115 (2020). http://doi.org/10.1186/s12951-020-00675-6